Materials Research Letters

ISSN: (Print) (Online) Journal homepage: https://www.tandfonline.com/loi/tmrl20

Tissue phase affected fracture toughness of nano-columnar TiB_{2+z} thin films

C. Fuger, R. Hahn, A. Hirle, T. Wojcik, P. Kutrowatz, F. Bohrn, O. Hunold, P. Polcik & H. Riedl

To cite this article: C. Fuger, R. Hahn, A. Hirle, T. Wojcik, P. Kutrowatz, F. Bohrn, O. Hunold, P. Polcik & H. Riedl (2023) Tissue phase affected fracture toughness of nano-columnar TiB_{2+z} thin films, Materials Research Letters, 11:8, 613-622, DOI: 10.1080/21663831.2023.2204120

To link to this article: https://doi.org/10.1080/21663831.2023.2204120

Published online: 26 Apr 2023.

MATER. RES. LETT.
2023, VOL. 11, NO. 8, 613–622
https://doi.org/10.1080/21663831.2023.2204120

MATERIALS RESEARCH LETTERS
Taylor & Francis
Taylor & Francis Group

ORIGINAL REPORTS

Tissue phase affected fracture toughness of nano-columnar TiB_{2+z} thin films

C. Fuger [a], R. Hahn [a], A. Hirle [a], T. Wojcik [a], P. Kutrowatz[a], F. Bohrn [a], O. Hunold[b], P. Polcik[c] and H. Riedl [a,d]

[a]Christian Doppler Laboratory for Surface Engineering of high-performance Components, TU Wien, Vienna, Austria; [b]Oerlikon Balzers, Oerlikon Surface Solutions AG, Balzers, Liechtenstein; [c]Plansee Composite Materials GmbH, Lechbruck am See, Germany; [d]Institute of Materials Science and Technology, TU Wien, Wien, Austria

ABSTRACT

Structural imperfections such as nano-columnar tissue phases constitute a morphological design feature in protective thin films. Especially in the rising group of PVD transition metal diborides, excess Boron is known to form nm-sized B-rich precipitations in-between nano-crystalline domains. Here, we focus on super-stoichiometric TiB_{2+z} thin films, varying the stoichiometry from $TiB_{2.04}$ to $TiB_{4.42}$ (B: 67–82 at.%). The tissue phase fraction and thickness is mainly governed by the B content and corresponding deposition conditions. A decreasing tissue phase width from ≈ 3–1 nm leads to an increasing critical stress intensity factor K_{IC} of ≈ 40%.

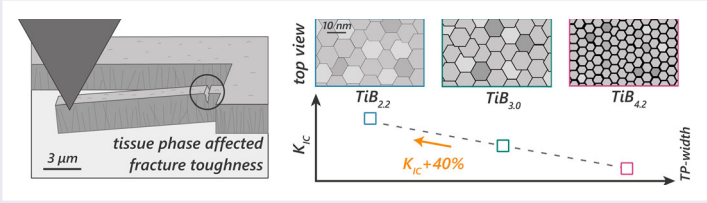

ARTICLE HISTORY
Received 1 December 2022

KEYWORDS
Transition metal diborides; TiB_2; tissue phase; micro-mechanical testing; fracture toughness

IMPACT STATEMENT

Tissue phase governed intrinsic fracture toughness (K_{IC}) of nano-crystalline TiB_{2+z} films with a maximum of 3.55 ± 0.16 MPa$\sqrt{m}$ for super-hard $TiB_{2.22}$.

Main section

Transition metal diborides (TMBs) attract much attention as their unique mix of properties offers great potential for diverse applications ranging from functional and protective thin films up to electrocatalysts [1,2]. Based on their electronegativity, lying between metals and non-metals, TMBs exist in a wide variety of crystal structures and stoichiometries. With the strongly limited kinetics during the most commonly used physical vapor deposition (PVD) technique, TMBs exhibit structural imperfections, such as point or line defects and tissue phases. Especially, superhard TiB_{2+z} is well known to form nm-sized precipitations in-between highly crystalline domains related to excess Boron available during PVD synthesis [3–6]. So far, tissue phases are also described for ZrB_2 and NbB_2, whereas surplus B accumulates in different 3-dimensional frameworks [5,7]. This B-rich tissue phase is an important morphological feature accounting for different phenomena, such as the volatile formation of B_2O_3 scales, poor oxidation resistance, and superior hardness due to impeded elasto-plastic deformation [8–10]. In detail, Mayrhofer et al. [3] ascribed the super hardness of $TiB_{2.4}$ to the grain separating B-rich tissue phase, inhibiting dislocation and grain-boundary gliding of the nano-columns. Based on ab-initio calculations, Kalfagiannis et al. [11] concluded that excess B in super-stoichiometric TiB_{2+z} exists as bulk B interstitials, small B clusters, but also as B-rich surface terminations, prohibiting grain boundary sliding. Palisaitis et al. investigated the sub-stoichiometric regime and identified B-deficient planar defects as a stabilizing contributor for α-structured (SG 191) TiB_2 [12].

However, tissue phase engineering for improving hardness is well-described for some material systems, e.g. nc-TiN/Si_3N_4 [13,14]. In contrast to hardness (H) and elastic modulus (E), only a small number of studies have focused on the intrinsic fracture toughness (K_{IC})

CONTACT C. Fuger christoph.fuger@tuwien.ac.at Christian Doppler Laboratory for Surface Engineering of high-performance Components, TU Wien, A-1060 Vienna, Austria

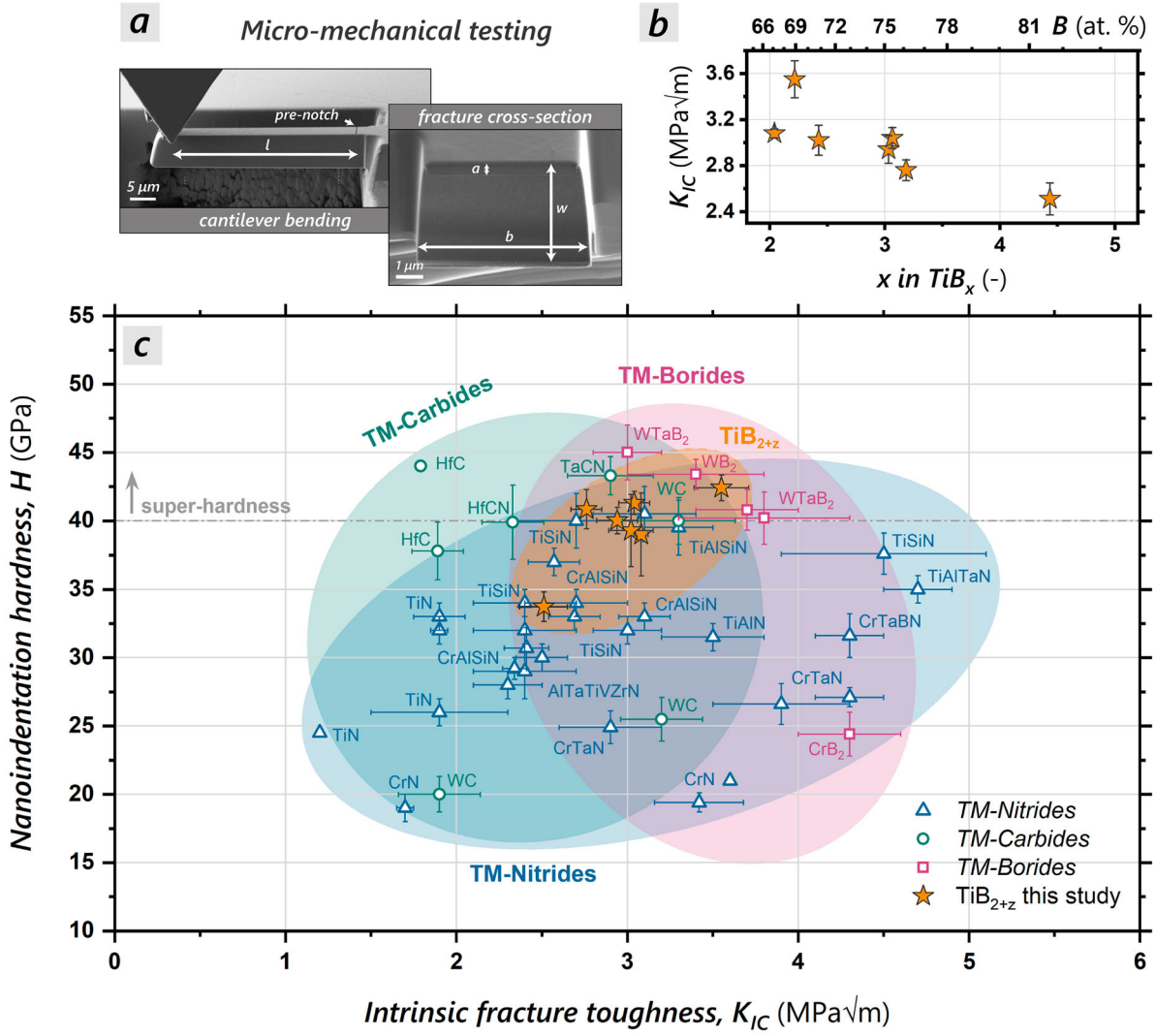

Figure 1. A FIB-manufactured $TiB_{3.06}$ micro-cantilever before a micro-mechanical bending test and the post-mortem fracture cross section is depicted in a. The resulting intrinsic K_{IC} values of TiB_x coatings with x = 2.04 - 4.42 are depicted in b. In c ceramic thin film material systems are classified by their intrinsic fracture toughness (K_{IC}) determined by micro-cantilever bending experiments and nanoindentation hardness values (H). The color-coded clouds indicate the associated material families marked in red (TM-Borides – red squares) [15,29], green (TM-Carbides – green circles) [26–28], and blue (TM-Nitrides – blue triangles) [16–25]. The obtained K_{IC} values of TiB_{2+z} from this study are marked in orange.

of TMBs in general, but even less on the influence of tissue phase dominated TMBs [15]. Figure 1c delineates K_{IC} (cantilever bending) and H values of various TM-nitride [16–25], TM-carbide [26–28], and TM-boride [15,29] based coatings. Thörnberg et al. [6] obtained K_C of various $TiB_{2\pm z}$ compositions by cube corner indentations. Here, the distinct influence of residual stresses due to the chosen methodology results in a more technologically significant characteristic value than intrinsic material property [6]. Nevertheless, recent advances make an accurate evaluation of K_{IC} for such small samples possible [30–33] and pave the way for a more detailed analysis of thin film fracture characteristics. Figure 1a shows a FIB fabricated $TiB_{3.06}$ cantilever before a micro-mechanical bending experiment and the post-mortem fracture cross-section. The indicated parameters l, a, b, w are essential for determining the K_{IC} value (for details see Methods section). In this work we correlate the constitution of the B-rich tissue phase in super-stoichiometric TiB_{2+z} (by detailed HR-TEM) with the fracture behavior obtained by micro-mechanics.

We synthesized super-stoichiometric TiB_{2+z} thin films by DC magnetron sputtering of a TiB_2 compound target. Due to mass disparities of Ar^+ ions (m_{Ar} = 39.95 u), sputtered B (m_B = 10.81 u) and Ti (m_{Ti} = 47.87 u) species, B is preferentially emitted along the target normal, while Ti follows a shallower distribution [4]. These collision-determined phenomena lead to a preferred deviation from stoichiometric TiB_2 and hence, excess B forming super-stoichiometric TiB_{2+z}.

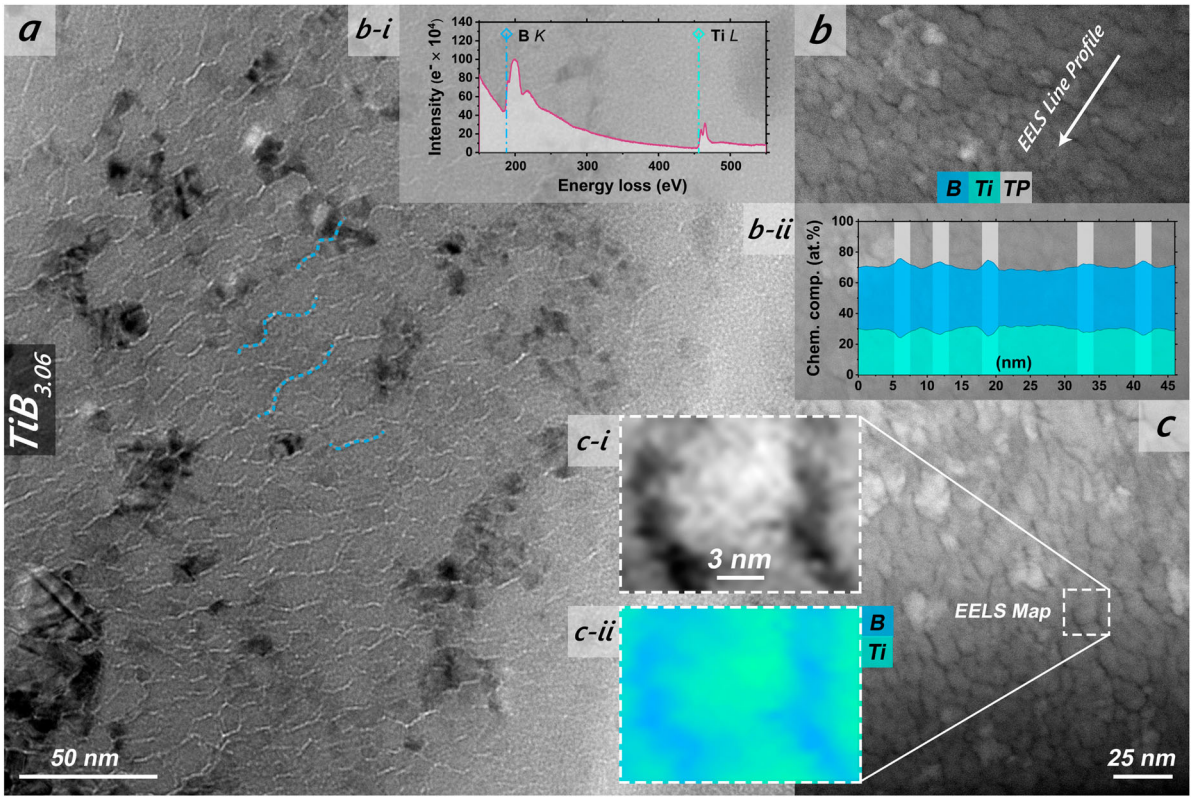

Figure 2. TEM top-view analysis of the $TiB_{3.06}$ coating: EF-TEM (a), STEM (b, c), and in-situ TEM-EELS was conducted (b-i, b-ii, c-ii). Section b-i depicts the electron energy loss spectrum used for the EELS line profile (white arrow in b) and indicates the B K edge at 188 eV (blue dashed line) and Ti L edge at 456 eV (green dashed line). Consequently, the resulting EELS line profile, represented in b-ii, shows detected B (blue area) and Ti (green area) – tissue phases (TP) are marked with grey areas. Section (c) shows an EELS mapping of a selected region (zoom-in in c-i). The detected elemental distribution reveals B-rich (blue) and Ti-rich (green) areas, presented in c-ii.

Nevertheless, the distribution of B and Ti orthogonal to the target surface can be specifically altered by varying pressure, distance, or the target-to-substrate angle. For $TiB_{2.04}$, $TiB_{2.22}$, $TiB_{2.43}$, $TiB_{3.03}$, $TiB_{3.19,}$ and $TiB_{4.42}$ the target and substrates were arranged parallel, while for $TiB_{3.06,}$ it was adjusted to $\approx$ 15°, see also Ref. [34]. All the investigated TiB_{2+z} films are highly 0001 oriented (see Figure A1), excluding a possible anisotropy effect. The predominant anisotropy of AlB_2 structured diborides [34,35] is underlined by micro-pillar compression experiments of $TiB_{3.06}$ thin films, leading to significantly higher engineering stress of the 0001 oriented coating compared to the thin film with mixed orientation (Figure A3). Moreover, as impurities are essential for tissue-phased engineered materials, we want to indicate that no oxide-based phases or clusters are detectable during structural analysis and SIMS measurements (see Figure A1 and A2).

In Figure 1b the intrinsic K_{IC} values of all deposited TiB_{2+z} films are depicted as a function of the B content. A change from 82 to 69 at.% Boron ($TiB_{4.42}$ to $TiB_{2.22}$) leads to an increase of around 40% from 2.51 ± 0.14–3.55 ± 0.16 MPa$\sqrt{m}$, respectively. Nevertheless, when taking into account the $TiB_{2.04}$ film with only 67 at.% B the increase in K_{IC} from $TiB_{4.42}$ to $TiB_{2.04}$ is 23% from 2.51 ± 0.14–3.08 ± 0.04 MPa$\sqrt{m}$. This deviation in K_{IC} increase unambiguously indicates that the amount of B is not the single key factor affecting the intrinsic K_{IC} of the TiB_{2+z} films.

TEM analysis of top-view prepared samples are conducted to understand the morphology of the formed tissue phases. In Figure 2a an EFTEM image of the $TiB_{3.06}$ coating is presented, exhibiting columns of $\approx$ 10 nm diameter, separated by thin ($\approx$ 1–2 nm) bright features representing the related tissue phase (lighter elements appear bright during EFTEM analysis – see also blue lines as guide for the eye). In contrast to EFTEM, light elements appear dark during STEM analysis (Z-contrast imaging), illustrated in Figure 2b and c. The electron energy loss spectrum (determined by EELS) of the $TiB_{3.06}$ film exhibits a characteristic B K edge at 188 eV (blue dashed line) and Ti L edge at 456 eV (green dash-dotted line), depicted in Figure 2b-i.

Consequently, an EELS line scan (white arrow in Figure 2b), unambiguously identifies B enriched areas on the column boundaries, hatched zones (TP) in

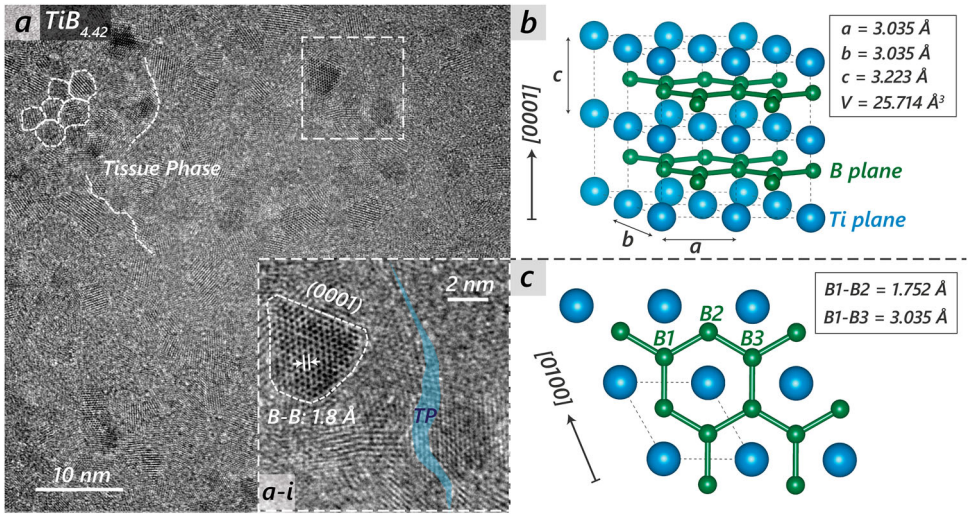

Figure 3. HR-TEM top view investigation of a $TiB_{4.42}$ thin film, providing insights into inter-atomic length scales. The dashed lines in a mark certain nano-columns separated by B-rich tissue phases. A zoom-in (dashed square in a, highlights the selected area) is depicted in a-i, showing an ideally 0001 oriented column, with visible B hexagons of a basal B plane of the hexagonal TiB_2 crystal lattice (SG191, P6mmm). Here, the measurements show an inter-atomic nearest B-B distance of 1.8 Å. The blue shaded area marks a $\approx$ 2 nm thick column-separating tissue phase (TP). In addition, b depicts a $2 \times 2 \times 2$ AlB_2 structured TiB_2 supercell, with lattice constants a, b, and c. Ti and B atoms are marked in blue and green, respectively. c shows the TiB_2 supercell with 0001 projection vector. B hexagons (also presented in a-i) from the B layer are visible, and B-B distances are delineated.

Figure 2b-ii. In addition, the EELS map in Figure 3c-i and c-ii highlights the elemental distribution of B and Ti in blue and green colors, featuring two broad B-rich tissue phases with a thickness of $\approx$ 2 nm.

Going even one step further, HR-TEM investigations of the $TiB_{4.42}$ thin film (also marked in Figure 4d) reveal insights into the nano-columnar morphology (surrounded by the tissue phase) down to atomistic length scales, see Figure 3. The $TiB_{4.42}$ coating exhibits crystalline columns with diameters $<$ 5 nm, surrounded by an amorphous tissue phase (appearing as bright features). In addition, certain column boundaries and tissue phases are traced by white dashed lines in the top left corner of Figure 3a. In the inset a-i, the blue shaded area indicates a $\approx$ 2 nm thick tissue phase. The white dashed line frames an ideally 0001 oriented column, where B hexagons of the hexagonal TiB_2 crystal lattice (SG191, P6mmm) are recognizable. The inter-atomic distance between the two nearest B atoms is $\approx$ 1.8 Å, being consistent with theoretical models (see Figure 3b and c). Based on these observations, the tissue phase in TiB_{2+z} is characterized as an amorphous but not solely B-containing region.

STEM visualizations of top view prepared $TiB_{2.22}$, $TiB_{2.43}$, $TiB_{3.06,}$ and $TiB_{4.42}$ coatings are summarized in Figure 4a-d comparing the tissue phase morphology of the different stoichiometries. A column diameter of $\approx$ 10 nm is detected for $TiB_{2.43}$ and $TiB_{3.06}$, underlined by EELS and HAADF (see Figure 4e-h and i-l). However, we observe drastic decreasing columns ($<$ 5 nm) for the $TiB_{4.42}$ stoichiometry (Figure 4d, h, l, as well as Figure 3). This behavior highlights that an increase of B does not necessarily lead to tissue phase broadening but to decreasing crystallite sizes of the nano-columns, providing an increased column boundary fraction for accumulating excess B atoms [34]. The inverse Hall Petch effect is the dominating hardening (softening) mechanism for such small grain size regimes ($<$ 10 nm), where grain boundary gliding is predominant with respect to dislocation movement [36,37]. Due to the V-shape nature of the columnar films and the smaller film thickness of the $TiB_{2.22}$ coating (see Table 1), the column size estimation by the STEM image (Figure 4a) is smaller ($\approx$ 5 nm) compared to $TiB_{2.43}$ and $TiB_{3.06}$.

In general, a decreasing B content is correlating with a decreasing tissue phase width and fraction, as depicted by the EELS line profiles in Figure 4e-h revealing decreasing B peak intensities for the tissue phases with decreasing B content. The HAADF profiles (Figure 4i-l) again highlight that darker regions on the STEM visualizations belong to the B-rich tissue phases, correlating with the B peaks of the EELS line spectra. However, in near stoichiometric regimes (B $<$ 70 at. %) also the deposition conditions (e.g. pressure) play a major role for the peculiarity of the tissue phase (see Figure A3). Increasing deposition pressure generally leads to a decreasing B content [34] but higher collision probability ergo less particle energy is suggested to be beneficial for the formation of amorphous B-rich tissue phases.

The results in this study suggest that the B content as well as deposition conditions (e.g. pressure) determine

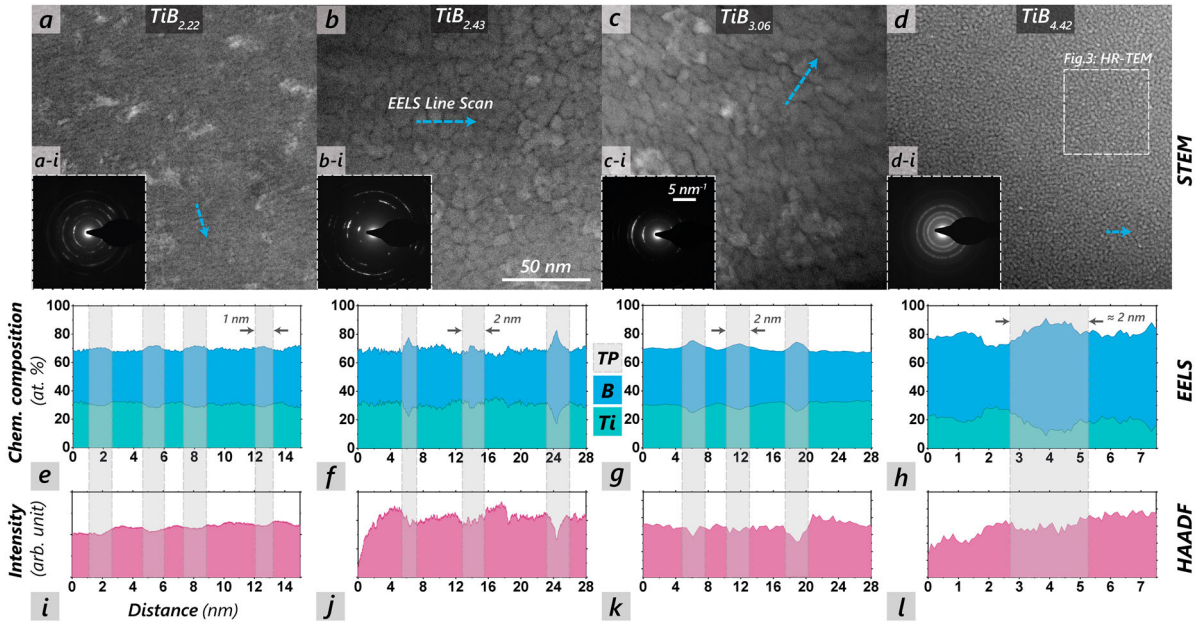

Figure 4. STEM analysis of top view prepared TiB_{2+z}, revealing nano-columnar morphologies of $TiB_{2.22}$ (a), $TiB_{2.43}$ (b), $TiB_{3.06}$ (c), and $TiB_{4.42}$ (d) thin films. The insets a-i, b-i, c-i and d-i represent in-situ TEM-SAED patterns in the reciprocal space of the corresponding coating. Sections e-h reveal the EELS line profiles from the marked areas (blue dashed arrows) in a-d. B is represented in blue and Ti in green, in correlation with the HAADF intensity profiles of section i-l. The sections in the EELS and HAADF spectra corresponding to the tissue phases (TP) are indicated in grey.

the formation of tissue phases, where smaller column sizes and an increased column boundary fraction are induced to distribute excess B. Crack propagation along tissue phases is suggested to be the predominant fracture mechanism, underlined by an intrinsic K_{IC} of 3.55 ± 0.16 for $TiB_{2.22}$ with smallest tissue phase width evaluated ($\approx$ 1 nm) and $2.51 \pm 0.14\,MPa\sqrt{m}$ for $TiB_{4.42}$ with $\approx$ 3 nm and, hence, highest tissue phase fraction due to smaller column size.

Methods

Film synthesis

An in-house developed DC balanced magnetron sputtering deposition system was used to synthesize the TiB_2 coating. The ultra-high vacuum coating facility was equipped with a 6-inch powder metallurgical produced TiB_2/C 99/1 wt.% target (purity > 99.6%). Before the depositions, the austenitic steel ($20 \times 7 \times 1$ mm^3) and sapphire ($10 \times 10 \times 0.53$ mm^3) substrates were ultrasonically pre-cleaned in acetone and ethanol for 5 min each. Subsequently, they were mounted on a rotating substrate holder (45°/s) on the inner (r = 35 mm) and outer radii (r = 70 mm), and heated (base pressure below $4 \cdot 10^{-4}$ Pa) to the deposition temperature, T_{sub}, of 500 ± 15 °C for 30 min. Furthermore, the substrates were etched in an argon atmosphere (p_{etch} = 6 Pa) for 10 min applying a substrate potential of −500 V. The deposition process was carried out in pure argon at a deposition pressure of 0.4 and 1.2 Pa, respectively. Moreover, the target substrate distance was set to 64, 104 and 124 mm – see Table 1. A schematic of the deposition setup is visualized in [34]. The TiB2/C target was powered by a Solvix HIP3 generator used in DC mode with a maximum current I_{target} of 4 A, leading to a 9 W/cm^2 power supply on the target.

The film growth was also supported by applying a negative BIAS potential of −50 V.

Table 1. Film stoichiometry and film thickness t, resulting from deposition pressure p_{dep}, target-substrate distance d_{dep}, substrate location on circular substrate holder r, deposition time t_{dep}, and cathode tilt.

Film stoichiometry	t(µm)	p_{dep}(Pa)	d_{dep} (mm)	r(mm)	t_{dep} (min)	cathodetilt (°)
$TiB_{2.04}$	2	1.2	64	70	45	0
$TiB_{2.22}$	2.5	0.4	64	70	45	0
$TiB_{2.43}$	5	1.2	104	70	150	0
$TiB_{3.03}$	6	1.2	104	35	150	0
$TiB_{3.06}$	5	0.4	104	70	150	15
$TiB_{3.19}$	5	0.4	124	35	160	0
$TiB_{4.42}$	6	0.4	124	70	160	0

Chemical and structural analysis

The elemental composition of the TiB_{2+z} films on sapphire substrates was analyzed by liquid inductively coupled plasma optical emission spectroscopy (ICP-OES) – for details see [34].

A Philips XPERT diffractometer in Bragg–Brentano configuration was used for detailed structural characterization. The diffractometer was equipped with a Cu-Kα ($\lambda = 1.54187$ Å) radiation source.

Nanoindentation

The hardness, H, and Young's modulus, E, of the coatings on austenitic steel substrate material were analyzed with an Ultra Micro Indentation System (UMIS). A three-sided Berkovich diamond tip (E = 1050 GPa and Poisson's ratio $\nu = 0.07$) was calibrated with a fused silica reference sample (E = 72.5 GPa, H = 10 GPa) – area function was obtained for a plastic depth of 69.6 nm. 35 indentations covering a force range from 10 to 45 mN were performed to establish the indentation properties of the TiB_2 film on an austenitic steel substrate. The resutling load-displacement curves were corrected with instrument compliance, initial penetration, and area function. Subsequently, the well-established approach from Oliver and Pharr [38] was used for evaluating H and E* of the TiB_2 film. A Poisson's ratio of $\nu = 0.15$ was adopted to calculate E out of the combined modulus and tip modulus.

Micromechanical testing

Seven micro-pillar geometries for compression tests, with a diameter of $\approx$ 2500 nm each, were produced by focused ion beam (FIB)-sputtering using a ThermoFisher Scios2 instrument. TiB_{2+z} on sapphire substrate was applied to ensure substrate influence was as low as possible due to the high stiffness of the subtrate. The geometries were prepared using a Ga-ion probe current of 15 nA for the rough cut down to 500 pA for the finishing step. Thereby, special attention was given to stopping the milling process directly at the coating-substrate interface. The pillar compression tests were performed in a Zeiss Sigma 500 VP FEGSEM combined with a Femto-Tools FT-NMT04 in-situ SEM nanoindenter equipped with a flat punch (5 µm diameter) diamond tip capable of applying 200 mN at a noise level of < 5 µN (measured at 10 Hz). The tests were carried out at room temperature in displacement-controlled mode with a displacement rate of 5 nm/s.

In situ micromechanical bending tests of substrate-free coating cantilevers were conducted to obtain the fracture toughness of the TiB_{2+z} coatings. The cantilevers of the TiB_{2+z} coatings on austenitic steel substrates were shaped by FIB milling, ensuring minimal FIB damage by reducing the final milling current to 1 nA. The initial notch was milled using an ion current of 50 pA. The experiments were performed with the same in-situ set up, using a wedge diamond tip to bend the pre-notched cantilever (in the growth direction of the coatings) until fracture. The calculation of the fracture toughness was performed after the linear elastic approach developed by Matoy et al. [30]. For the fracture toughness evaluation, the following equation was used:

$$K_{IC} = \frac{P_{max} l}{b w^{\frac{3}{2}}} \left(1.46 + 24.36\left(\frac{a}{w}\right) - 47.21\left(\frac{a}{w}\right)^2 + 75.18\left(\frac{a}{w}\right)^3\right) \quad (1)$$

with P_{max} being the maximum force during loading, l the cantilever length, b, the width, w the height, and a the initial notch depth. The cantilever dimensions were determined using the above-mentioned SEM. We performed at least 5 successful experiments per sample state.

Transmission electron microscopy

Detailed microstructure investigations have been performed using a TEM, FEI TECNAI F20, equipped with a field emission gun and operated at an accelerating voltage of 200 kV. Energy-filtered TEM (EFTEM), scanning-TEM (STEM), and selected area electron diffraction (SAED) were applied to reveal nano-crystalline morphologies, crystal structure, and texture of the investigated TiB_{2+z} coatings on austenitic steel substrates. Electron energy loss spectrum (EELS) analysis was conducted to determine the distribution of light B and heavy Ti elements down to a spatial resolution of 1 nm. The TEM top view samples were prepared using the standard FIB lift-out method on a selected surface-near region.

Acknowledgements

The financial support by the Austrian Federal Ministry for Digital and Economic Affairs, the National Foundation for Research, Technology and Development and the Christian Doppler Research Association is gratefully acknowledged (Christian Doppler Laboratory "Surface Engineering of high-performance Components"). We also thank for the financial support of Plansee SE, Plansee Composite Materials GmbH, and Oerlikon Balzers, Oerlikon Surface Solutions AG. In addition, we want to thank the X-ray center (XRC) of TU Wien for beam time as well as the electron microscopy center - USTEM TU Wien - for using the TEM facility. The authors acknowledge TU Wien Bibliothek for financial support through its Open Access Funding Program.

Author contributions

C. F., R. H., and H. R. conceived the research. C. F., R.H., and A.H. conducted the depositions, structural, and mechanical investigations. T. W. performed the HR-TEM analysis. P. K. TEM sample preparation. F.B. conducted the SIMS analysis. P. P. and O. H. supported the

research by providing funding and expertise. H. R. supervised the project, and provided the funding. All authors then contributed and have given approval to the final version of the manuscript.

Disclosure statement

No potential conflict of interest was reported by the author(s).

ORCID

C. Fuger http://orcid.org/0000-0003-2685-4808
R. Hahn http://orcid.org/0000-0002-7322-8108
A. Hirle http://orcid.org/0000-0003-0345-6962
T. Wojcik http://orcid.org/0000-0001-5091-5215
F. Bohrn http://orcid.org/0000-0002-0288-3359
H. Riedl http://orcid.org/0000-0002-8108-1185

References

[1] Magnuson M, Hultman L, Högberg H. Review of transition-metal diboride thin films. Vacuum. 2022;196:110567.
[2] Yao Y, Zhang Z, Jiao L. Development strategies in transition metal borides for electrochemical water splitting. Energy Environ Mater. 2021;5:470–485.
[3] Mayrhofer PH, Mitterer C, Wen JG, et al. Self-organized nanocolumnar structure in superhard TiB2 thin films. Appl Phys Lett. 2005;86(13):1–3.
[4] Neidhardt J, Mráz S, Schneider JM, et al. Experiment and simulation of the compositional evolution of Ti–B thin films deposited by sputtering of a compound target. J Appl Phys. Sep. 2008;104(6):63304.
[5] Schnitter C, Petrov I, Zhirkov I, et al. Effect of low-energy ion assistance on the properties of sputtered ZrB2 films. Vacuum. 2021;195(October):110688.
[6] Thörnberg J, Palisaitis J, Hellgren N, et al. Microstructure and materials properties of understoichiometric TiBx thin films grown by HiPIMS. Surf Coatings Technol. 2020;404(October).
[7] Nedfors N, Tengstrand O, Lu J, et al. Superhard NbB2 −x thin films deposited by dc magnetron sputtering. Surf Coatings Technol. Oct. 2014;257:295–300.
[8] Berger M, Karlsson L, Larsson M, et al. Low stress TiB2 coatings with improved tribological properties. Thin Solid Films. 2001;401(1–2):179–186.
[9] Mikula M, Grančič B, Roch T, et al. The influence of low-energy ion bombardment on the microstructure development and mechanical properties of TiBx coatings. Vacuum. 2011;85(9):866–870.
[10] Bakhit B, Palisaitis J, Thörnberg J, et al. Improving the high-temperature oxidation resistance of TiB2 thin films by alloying with Al. Acta Mater. 2020;196:677–689.
[11] Kalfagiannis N, Volonakis G, Tsetseris L, et al. Excess of boron in TiB2 superhard thin films: A combined experimental and ab initio study. J Phys D Appl Phys. 2011;44(38).
[12] Palisaitis J, Dahlqvist M, Hall AJ, et al. Where is the unpaired transition metal in substoichiometric diboride line compounds? Acta Mater. 2021;204:116510.
[13] Veprek S. Recent search for new superhard materials: Go nano!. J Vac Sci Technol A Vacuum, Surfaces, Film. 2013;31(5):50822.
[14] Veprek S, Karvankova P, Veprek-Heijman MGJ. Possible role of oxygen impurities in degradation of nc-Ti N/ a-Si 3 N 4 nanocomposites. J Vac Sci Technol B Microelectron Nanom Struct Process Meas Phenom. 2005;23(6):L17–L21.
[15] Fuger C, Moraes V, Hahn R, et al. Influence of Tantalum on phase stability and mechanical properties of WB2. MRS Commun. Mar. 2019;9(01):375–380.
[16] Daniel R, Meindlhumer M, Zalesak J, et al. Fracture toughness enhancement of brittle nanostructured materials by spatial heterogeneity: a micromechanical proof for CrN/Cr and TiN/SiOx multilayers. Mater Des. 2016;104:227–234.
[17] Liu S, Wheeler JM, Davis CE, et al. The effect of Si content on the fracture toughness of CrAlN/Si3N4 coatings. J Appl Phys. 2016;119(2):25305.
[18] Bartosik M, Hahn R, Zhang ZL, et al. Fracture toughness of Ti-Si-N thin films. Int J Refract Met Hard Mater. 2018;72(October 2017):78–82.
[19] Bartosik M, Rumeau C, Hahn R, et al. Fracture toughness and structural evolution in the TiAlN system upon annealing. Sci Rep. 2017;7(1):1–9.
[20] Hahn R, Kirnbauer A, Bartosik M, et al. Toughness of Si alloyed high-entropy nitride coatings. Mater Lett. 2019;251:238–240.
[21] Moritz Y, Kainz C, Tkadletz M, et al. Microstructure and mechanical properties of arc evaporated Ti(Al,Si)N coatings. Surf Coatings Technol. 2021;421:127461.
[22] Kainz C, Pohler M, Tkadletz M, et al. The influence of bias voltage on structure, thermal stability and mechanical properties of arc evaporated Cr0.69Ta0.20B0.11N coatings. Surf Coatings Technol. 2021;428(September):127867.
[23] Best JP, Zechner J, Wheeler JM, et al. Small-scale fracture toughness of ceramic thin films: the effects of specimen geometry, ion beam notching and high temperature on chromium nitride toughness evaluation. Philos Mag. 2016;96(32–34):3552–3569.
[24] Seidl WM, Bartosik M, Kolozsvári S, et al. Influence of Ta on the fracture toughness of arc evaporated Ti-Al-N. Vacuum. 2018;150:24–28.
[25] Sperr M, Zhang ZL, Ivanov YP, et al. Correlating elemental distribution with mechanical properties of TiN/SiNx nanocomposite coatings. Scr Mater. 2019;170:20–23.
[26] Glechner T, Lang S, Hahn R, et al. Correlation between fracture characteristics and valence electron concentration of sputtered Hf-C-N based thin films. Surf Coatings Technol. 2020;399(July):126212.
[27] Glechner T, Hahn R, Zauner L, et al. Structure and mechanical properties of reactive and non-reactive sputter deposited WC based coatings. J Alloys Compd. 2021;885:161129.
[28] Glechner T, Hahn R, Wojcik T, et al. Assessment of ductile character in superhard Ta-C-N thin films. Acta Mater. Oct. 2019;179:17–25.
[29] Zauner L, Hahn R, Aschauer E, et al. Assessing the fracture and fatigue resistance of nanostructured thin films. Acta Mater. 2022;239:118260.

[30] Matoy K, Schönherr H, Detzel T, et al. A comparative micro-cantilever study of the mechanical behavior of silicon based passivation films. Thin Solid Films. 2009;518(1):247–256.
[31] Brinckmann S, Matoy K, Kirchlechner C, et al. On the influence of microcantilever pre-crack geometries on the apparent fracture toughness of brittle materials. Acta Mater. Sep. 2017;136:281–287.
[32] Brinckmann S, Kirchlechner C, Dehm G. Stress intensity factor dependence on anisotropy and geometry during micro-fracture experiments. Scr Mater. 2017;127:76–78.
[33] Pippan R, Wurster S, Kiener D. Fracture mechanics of micro samples: Fundamental considerations. Mater Des. 2018;159:252–267.
[34] Fuger C, Hahn R, Hirle A, et al. Revisiting the origins of super-hardness in TiB2 + z thin films – Impact of growth conditions and anisotropy. Surf Coatings Technol. 2022:128806.
[35] Fuger C, Hahn R, Zauner L, et al. Anisotropic superhardness of hexagonal WB2 ± z thin films. Mater Res Lett. 2022;10(2):70–77.
[36] Schiøtz J, Di Tolla FD, Jacobsen KW. Softening of nanocrystalline metals at very small grain sizes. Nature. 1998;391(6667):561–563.
[37] Zhang S, Sun D, Fu Y, et al. Recent advances of superhard nanocomposite coatings: a review. Surf Coatings Technol. 2003;167(2–3):113–119.
[38] Oliver WC, Pharr GM. An improved technique for determining hardness and elastic modulus using load and displacement sensing indentation experiments. J Mater Res. 1992;7(6):1564–1583.

Appendix

Figure A1. includes the diffraction pattern of the used TiB_2/C target, placed at the very bottom. Due to the high oxygen affinity of Ti/TiB_2 based powders, small fractions of O are naturally present within these raw materials, and therefore distinguishable in small amounts as cubic TiO (red dotted lines and red circles) within the target.

A TOF-SIMS 5 instrument (IONTOF GmbH, Münster, Germany) was used. Depth profiles were acquired in a high vacuum ($\approx$ 4·10-9 mbar) using a 25 keV Bi + primary ion beam. Two different measurement modes were used. High current bunched mode (HCBU) was used for depth profile measurements requiring a high mass resolution and low detection limit. As non-metal elements were the focus of the research, a 2 keV Cesium was used as the sputter gun, and the polarity was set to negative.

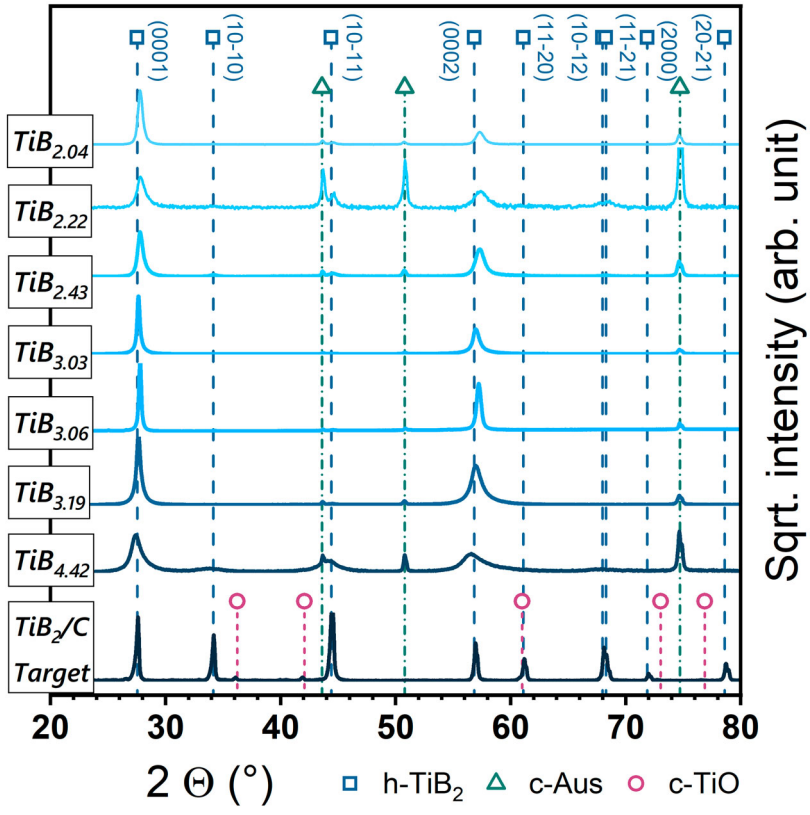

Figure A1. Characteristic pattern arising from X-Ray diffraction on the TiB_{2+z} highly crystalline domains. The TiB_{2+z} thin films on austenitic steel substrates are arranged by their B content, increasing from top to bottom (x = 2.04–4.42). For comparison, the diffraction pattern of the used TiB_2/C 99/1 wt.% 6" target is plotted at the very bottom. The reference patterns for hexagonal TiB_2 (SG191, P6mmm), cubic austenite (SG225, Fm-3 m), and cubic TiO (SG225, Fm-3 m) are indicated by blue squares, green triangles, and red circles, respectively.

Table A1. Elemental composition from ICP-OES analysis and mechanical properties of the synthesized TiB_{2+z} thin films.

Film stoichiometry	B(at.%)	Ti(at.%)	H(GPa)	E(GPa)	H^3/E^2(GPa)	K_{IC}(MPa$\sqrt{m}$)
$TiB_{2.04}$	67.1	32.9	39.0 ± 3.0	413 ± 15	0.35	3.08 ± 0.04
$TiB_{2.22}$	68.9	31.1	42.4 ± 0.9	424 ± 6	0.42	3.55 ± 0.16
$TiB_{2.43}$	70.8	29.2	39.3 ± 2.6	476 ± 28	0.27	3.02 ± 0.13
$TiB_{3.03}$	75.2	24.8	40.1 ± 1.0	445 ± 12	0.33	2.94 ± 0.12
$TiB_{3.06}$	75.4	24.6	41.3 ± 0.9	448 ± 10	0.35	3.04 ± 0.09
$TiB_{3.19}$	76.1	23.9	40.8 ± 1.4	409 ± 13	0.41	2.76 ± 0.09
$TiB_{4.42}$	81.6	18.4	33.7 ± 1.1	364 ± 14	0.29	2.51 ± 0.14

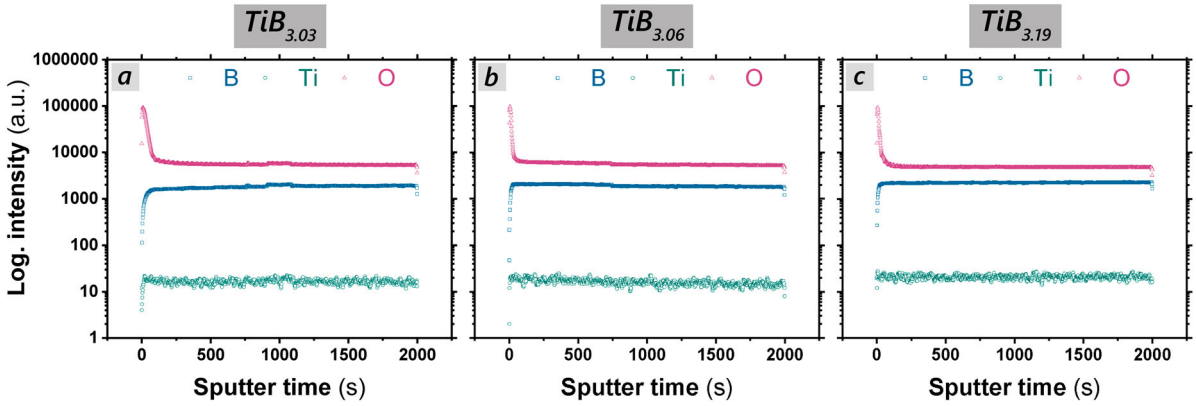

Figure A2. SIMS analysis of a $TiB_{3.03}$ (a), $TiB_{3.06}$ (b), and $TiB_{3.19}$ (c) thin film. Sputtered B, Ti, and O atoms are depicted as a function of sputter time t, by blue squares, green circles, and red triangles, respectively. We acquired a depth profile in HCBU mode with a fov (field-of-view) of 100 × 100 µm at 128 × 128 px in interlaced mode, set the used sputter gun to 300 × 300 µm, and limited the measurement duration to 2000 s [1-4]. Low energy electron flooding of 21 V is used to reduce surface charging.

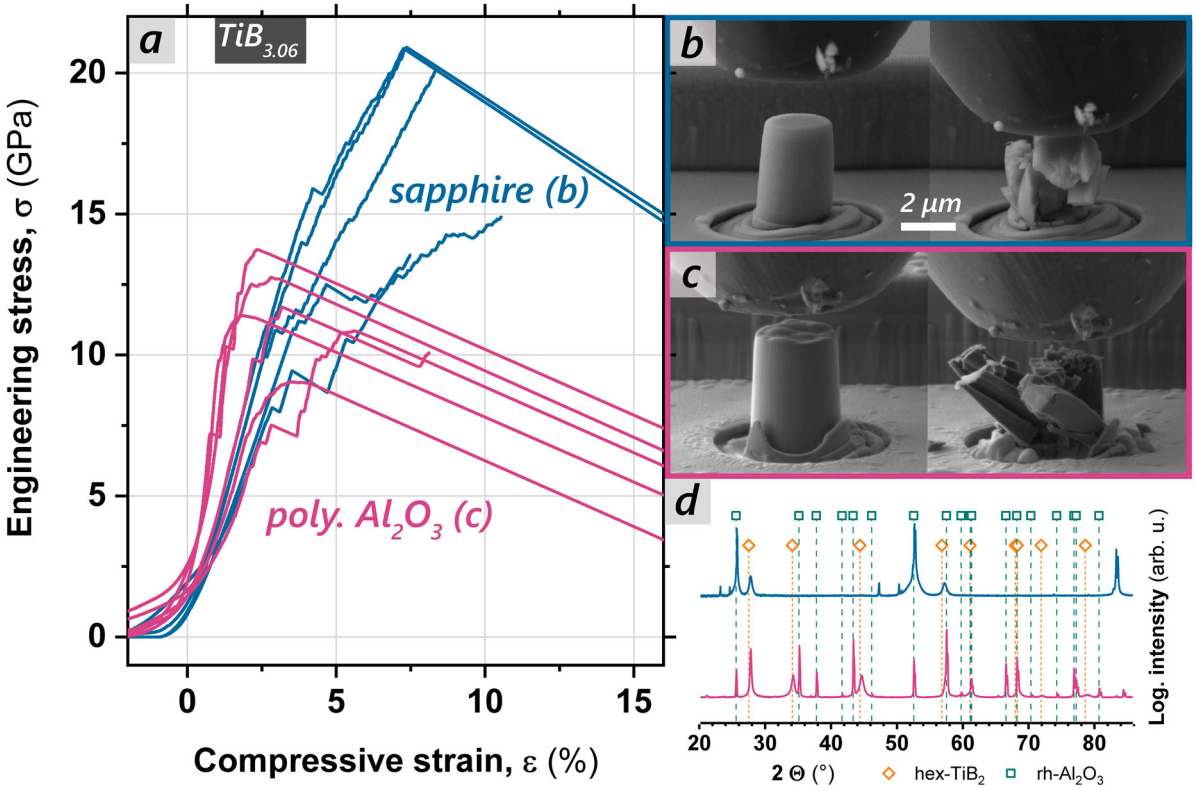

Figure A3. (a) Stress-strain data obtained by micro-pillar compression experiments of $TiB_{3.06}$ thin films. The blue curves correspond to 0001 oriented $TiB_{3.06}$ on sapphire substrate (b) material. $\sigma - \epsilon$ data from randomly oriented $TiB_{3.06}$ on polycrystalline Al_2O_3 substrate (c) is represented by red curves. Section d depicts the XRD pattern of the $TiB_{3.06}$ coating on sapphire (blue pattern) and polycrystalline Al_2O_3 (red pattern).

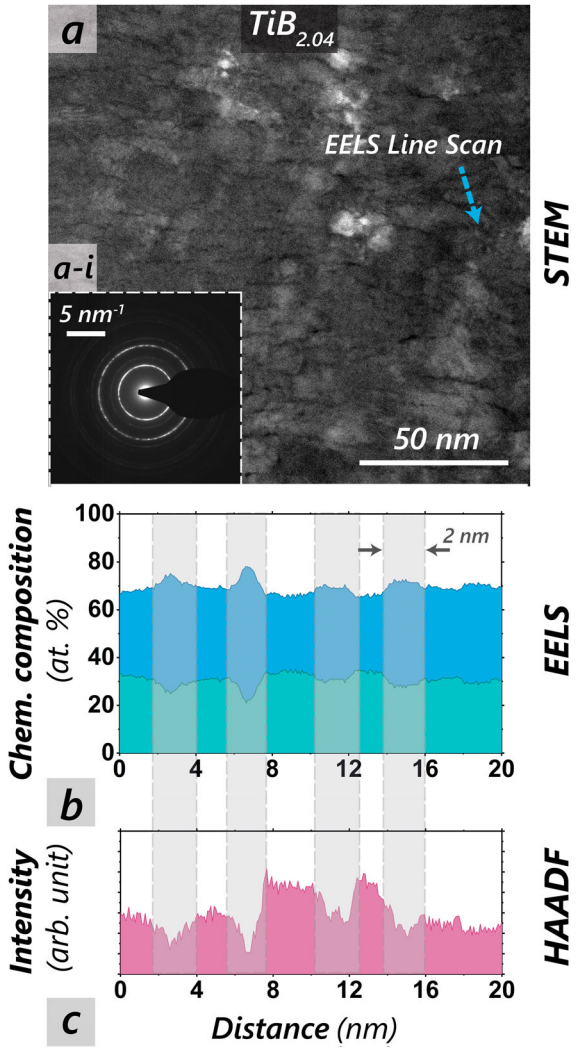

Figure A4. STEM analysis of top view prepared $TiB_{2.04}$. The inset a-i represents an in-situ TEM-SAED pattern in the reciprocal space of the corresponding coating. EELS line profiles from the marked area (blue dashed arrow) in a are depicted in b. B is represented in blue and Ti in green, in correlation with the HAADF intensity profile of section c. The sections in the EELS and HAADF spectra corresponding to the tissue phases (TP) are indicated in grey.

References

[S1] Benninghoven, A. Surface Analysis by Secondary Ion Mass Spectrometry (SIMS). Surf. Sci. 1994, 299-300, 246–260. https://doi.org/10.1016/0039-6028(94)90658-0.

[S2] Benninghoven, A. Chemical Analysis of Inorganic and Organic Surfaces and Thin Films by Static Time-of-Flight Secondary Ion Mass Spectrometry (TOF-SIMS). Angewandte Chemie International Edition in English. 1994, pp 1023–1043. https://doi.org/10.1002/anie.199410231.

[S3] Kubicek, M.; Holzlechner, G.; Opitz, A. K.; Larisegger, S.; Hutter, H.; Fleig, J. A Novel ToF-SIMS Operation Mode for Sub 100 Nm Lateral Resolution: Application and Performance. Appl. Surf. Sci. 2014, 289 (100), 407–416. https://doi.org/10.1016/j.apsusc.2013.10.177.

[S4] Sodhi, R. N. S. Time-of-Flight Secondary Ion Mass Spectrometry (TOF-SIMS):—versatility in Chemical and Imaging Surface Analysis. Analyst 2004, 129 (6), 483–487. https://doi.org/10.1039/B402607C.